

Anisotropic Convection Model for the Earth's Mantle

H.-B. Mühlhaus^{1,2}, M. Čada³, and L. Moresi⁴

¹ The University of Queensland
St Lucia, QLD 4072, Australia
`muhlhaus@quakes.uq.edu.au`

² CSIRO Division of Exploration and Mining
26 Dick Perry Ave., Kensington WA 6051, Australia

³ Ludwig-Maximilians University, Institute of Geophysics
Theresienstr. 41, 80333 Munich, Germany
`miro.cada@addcom.de`

⁴ School of Mathematical Sciences, Building 28, Monash University
Victoria 3800, Australia
`louis.moresi@sci.monash.edu`

Abstract. The paper presents a theory for modeling flow in anisotropic, viscous rock. This theory has originally been developed for the simulation of large deformation processes including the folding and kinking of multi-layered visco-elastic rock (Mühlhaus et al. [1,2]). The orientation of slip planes in the context of crystallographic slip is determined by the normal vector – the director – of these surfaces. The model is applied to simulate anisotropic mantle convection. We compare the evolution of flow patterns, Nusselt number and director orientations for isotropic and anisotropic rheologies. In the simulations we utilize two different finite element methodologies: The Lagrangian Integration Point Method Moresi et al [8] and an Eulerian formulation, which we implemented into the finite element based pde solver Fastflo (www.cmis.csiro.au/Fastflo/). The reason for utilizing two different finite element codes was firstly to study the influence of an anisotropic power law rheology which currently is not implemented into the Lagrangian Integration point scheme [8] and secondly to study the numerical performance of Eulerian (Fastflo)- and Lagrangian integration schemes [8]. It turned out that whereas in the Lagrangian method the Nusselt number vs time plot reached only a quasi steady state where the Nusselt number oscillates around a steady state value the Eulerian scheme reaches exact steady states and produces a high degree of alignment (director orientation locally orthogonal to velocity vector almost everywhere in the computational domain). In the simulations emergent anisotropy was strongest in terms of modulus contrast in the up and down-welling plumes. Mechanisms for anisotropic material behavior in the mantle dynamics context are discussed by Christensen [3]. The dominant mineral phases in the mantle generally do not exhibit strong elastic anisotropy but they still may be oriented by the convective flow. Thus viscous anisotropy (the main focus of this paper) may or may not correlate with elastic or seismic anisotropy.

1 Introduction

Layered rock structures typically exhibit spectacular deformation patterns, illustrations of buckling phenomena on a massive scale. Layered or, more generally, transversely

isotropic materials are indeed ubiquitous in the lithosphere ("the plate"). There is also mounting evidence (mainly from seismic measurements) that at least the upper part of the mantle exhibits acoustic wave anisotropy. A model for a layered mantle was proposed recently e.g. by Aki [5] and Takeuchi et al. [8]. Physical explanations for the presence of material anisotropy in the mantle may be based on flow alignment of the crystallographic slip planes of olivine (the dominant mineral in the mantle). Indeed, laboratory studies by Karato [6] in the context of flow alignment and seismic anisotropy have revealed two classes of anisotropy namely lattice preferred orientation and shape preferred orientation. Hence the proper consideration of the spatial orientation of the dominant slip plane as well as its kinematic and dynamic properties are crucial for the simulation of anisotropic mantle convection.

So far direct simulations of anisotropic mantle flows have been a highly specialized area (e.g. Christensen [3]; the paper also contains concise summary of possible mechanisms for anisotropic behavior). A possible reason may be that conclusive seismic anisotropy data have become available only relatively recently. In the following we give brief outlines of the constitutive theory [1,2] and the Lagrangian Integration Point finite element scheme (LIP), which we used for the solution of the example problems. Our LIP based code allows only linear strain rate dependency at present. In order to study the influence of a power law rheology on the evolution of viscous anisotropy we have implemented the governing equations into a finite element based partial differential equation solver package (Sect. 4). Results including comparisons of anisotropic and isotropic natural convection in a unit cell are presented in the Sects. 3 and 4. The question remains if there is a relationship between elastic (seismic) and viscous anisotropy. If the anisotropy is due to an alternating sequence of mineralogically and mechanically distinct constituents (Allegre and Turcotte, 1986) then the answer is yes; although the elastic strength of the anisotropy in terms of moduli contrast may differ from the viscosity contrast. If the seismic anisotropy is related to the elastic anisotropy in single crystals then the question is whether the reorientation of the crystallographic lattice is described sufficiently accurately by the evolution of the single director (normal vector) of the dominant slip system (Eq. (3)). In single slip and if elastic deformations are negligible this should be the case.

2 Mathematical Formulation

In the case of a material with layering or preferred crystallographic slip directions, the orientation of the director is normal to the layer or slip surfaces. Transverse-isotropic relations are characterized by two effective viscosities. We designate normal viscosity as η ($\sigma_{11} = -p + 2\eta D'_{11}$) and η_s ($\sigma_{12} = 2\eta_s D'_{12}$) is the shear viscosity. In the following simple model for a layered viscous material we correct the isotropic part $2\eta D'_{ij}$ of the model by means of the A_{ijkl} tensor (Mühlhaus et al. [1,2]) to consider the mechanical effect of the layering; thus

$$\sigma_{ij} = 2\eta D'_{ij} - 2(\eta - \eta_s)A_{ijlm}D'_{lm} - p\delta_{ij} \quad (1)$$

where a prime designates the deviator of the respective quantity, p is the pressure, D_{ij} is the stretching, σ_{ij} is the Cauchy or true stress and

$$A_{ijkl} = \frac{1}{2}(n_i n_k \delta_{lj} + n_j n_k \delta_{il} + n_i n_l \delta_{kj} + n_j n_l \delta_{ik}) - 2n_i n_j n_k n_l. \quad (2)$$

is the anisotropy tensor. In (1) and (2) the vector n_i is the unit orientation-vector of the director N_i . In the present applications we assume that the director transforms as a material surface element; in continuum mechanics theory the evolution of the director of the layers can be derived through the time derivative of Nanson's equation, which relates the current director to the reference director:

$$\dot{N}_i = N_{i,t} + v_j N_{i,j} = -v_{j,i} N_j \quad (3)$$

where v_i is the velocity vector. In 2D it is plausible that the planes of anisotropy or slip planes are aligned with the velocity vectors in steady states, which is equivalent to normality of the directors to the velocity vectors.

2.1 Numerical Method

The Lagrangian Integration Point finite element method ELLIPSIS uses a standard mesh to discretize the domain into elements, and the shape functions interpolate node points in the mesh in the usual fashion. Derivatives are computed on the mesh using the values of nodal variables but material property variations like the "director" are measured by the particles. The problem is formulated in a weak form to give an integral equation, and the shape function expansion produces a discrete (matrix) equation. For the discretized problem, these integrals occur over sub-domains (elements) and are calculated by summation over a finite number of sample points (tracers) within each element. For example, in order to integrate the components of the element stiffness matrix \mathbf{K}^E over the element domain Ω^E :

$$\mathbf{K}^E = \int_{\Omega^E} \mathbf{B}^T(\mathbf{x}) \mathbf{C}(\mathbf{x}) \mathbf{B}(\mathbf{x}) d\Omega \quad (4)$$

we replace the continuous integral by a summation

$$\mathbf{K}^E = \sum_p w_p \mathbf{B}_p^T(\mathbf{x}_p) \mathbf{C}_p(\mathbf{x}_p) \mathbf{B}_p(\mathbf{x}_p) \quad (5)$$

Here the matrix \mathbf{B} consists of the appropriate gradients of interpolation functions which transform nodal point velocity components to strain-rate pseudo-vectors at any points in the element domain. \mathbf{C} the constitutive operator corresponding to (1) is composed of two parts $\mathbf{C} = \mathbf{C}_{iso} + \mathbf{C}_{aniso}$.

In standard finite elements, the positions of the sample points, \mathbf{x}_p , and the weighting, w_p are optimized in advance. In our scheme, the \mathbf{x}_p 's correspond precisely to the Lagrangian points embedded in the fluid, and w_p must be recalculated at the end of a time-step for the new configuration of particles. The Lagrangian points carry the history variables

(in this case director orientation) which are therefore directly available for the element integrals without the need to interpolate from nodal points to fixed integration points. Moresi et al. [9] give a full discussion of the implementation and integration scheme.

In the Fastflo based simulations (www.cmis.csiro.au/Fastflo/) the advection terms in the heat equation and in the purely hyperbolic director evolution equation are stabilized using artificial diffusion terms a method which is also called tensor upwinding (Zienkiewicz and Taylor, [10]). See Sect. 4 for more details.

3 Application

We have simulated a basally heated convection problem in a box of aspect ratio 2×1 , with free slip-boundary conditions where the temperature is fixed at the top and bottom and there is no heat flux at the sides. We assume a Rayleigh-number of $Ra = 5.64 \times 10^5$ and a constant ratio of $\frac{\eta}{\eta_S} = 10$ (Fig. 1). Subsequently the influence of the viscosity ratio on the time history of the Nusselt number is also investigated (Fig. 2). In the definition of the Rayleigh number for anisotropic viscous materials we follow Christensen [3] and

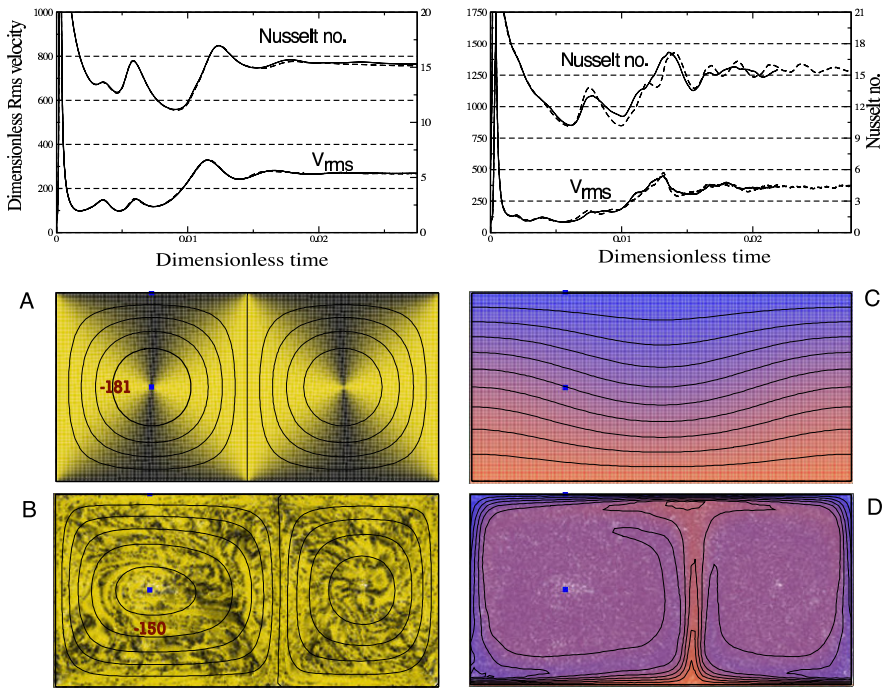


Fig. 1. Time dependent convection in a 2×1 box. $Ra = 5.6 \times 10^5$. Time series plots of velocity and Nusselt number isotropic convection (top left) and anisotropic convection, $\frac{\eta_S}{\eta}$ (top right). Dashed lines and lines are the results of the 32×32 and 64×64 elements simulations respectively. The initial state of alignment is shown in (a) and the initial thermal structure in (b), and after 4000 time-steps ($t = 0.04$) in (c) and (d)

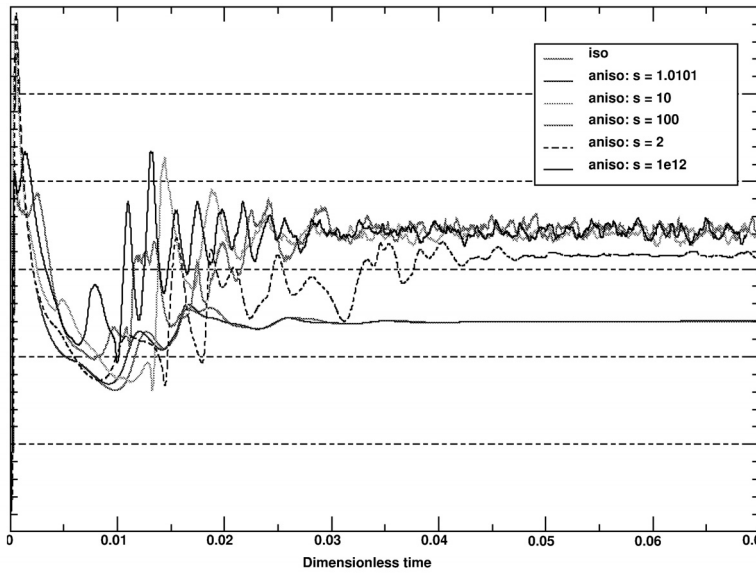


Fig. 2. Nusselt no. plots for different viscosity ratios: $s = \eta/\eta_S$

define:

$$Ra = \frac{2\alpha\rho_0^2 c_p g \Delta T H^3}{\kappa(\eta + \eta_s)} \quad (6)$$

The results suggest that the boundary layers in anisotropic convection are somewhat more stable than the equivalent isotropic boundary layers in medium to high Ra convection, leading to a reduced tendency for convection cells to break down and reform. The isotropic simulation passes through different stages of convective evolution, displaying plumes of hot material raising and cold material descending into its core, until two dominant convection cell emerge and persist in the steady state shown in Fig. 1. In the orthotropic simulation the director evolution follows the induced shear, and director alignment in rising plumes as well as director alignment in the boundary layers is visible in steady state. These aligned regions encircle a core of roughly randomly oriented directors. This suggests that seismic anisotropy is likely to be mostly dominant in up and down welling plumes and the hot and cold thermal boundary layers where shear-strain rates are high. This fits the observational evidence that deep mantle anisotropy is significant smaller, than in the shallow lithosphere (upper boundary layer) or the 660 km discontinuity and even the D'' layer (Montagner and Kennett [7]). Nusselt number histories for varying viscosity ratios are depicted in Fig. 2. It turns out that the graphs don't differ much for $\frac{\eta}{\eta_S} > 10$ i.e. there is little difference between the histories for the ratios 10, 100 and 10^{12} .

4 Power Law Induced Anisotropy

In this section we investigate the influence of a power law rheology on the spatial distribution of the strength of the anisotropy as expressed by the local value of the ratio η/η_S . The behavior is locally isotropic if the viscosity ratio is equal to 1; the most extreme case of anisotropy would correspond to a ratio of ∞ (see Fig. 2), where we have plotted the Nusselt-number of different viscosities ratios). In the study we use the simple relationship

$$\frac{\eta}{\eta_S} = (1 + \dot{\gamma}/\dot{\gamma}_Y)^{1-\frac{1}{n}}, \quad (7)$$

where in general $\dot{\gamma}$ is defined as:

$$\dot{\gamma} = \sqrt{D_{ij} \Lambda_{ijkl} D_{kl}} \quad (8)$$

In 2D there is a simpler way to calculate $\dot{\gamma}$: The shear strain vector on the N slip surface is:

$$\dot{\gamma}_i = D_{ij} n_j \quad (9)$$

Let \mathbf{m} be a vector in the slip plane so that $\mathbf{m} \cdot \mathbf{n} = 0$. In 2D the components of \mathbf{m} read:

$$\mathbf{m} = \begin{pmatrix} n_2 \\ -n_1 \end{pmatrix} \quad (10)$$

The magnitude of the shear stress on the n -surface is then defined as:

$$\dot{\gamma} = |D_{ij} n_j m_i| = |n_1 n_2 (D_{11} - D_{22}) + D_{12} (n_2^2 - n_1^2)| \quad (11)$$

The parameter $\dot{\gamma}_Y$ is a strain rate characterizing the transition from predominantly linear creep to power law creep and the superscript n is the power law exponent. We find the following limit values for the viscosity ratio:

$$\lim_{\dot{\gamma} \rightarrow 0} \left(\frac{\eta}{\eta_S} \right) = 1 \quad (12)$$

$$\lim_{\dot{\gamma} \rightarrow \infty} \left(\frac{\eta}{\eta_S} \right) = \infty \quad (13)$$

We consider a quadratic convection cell with ideal frictionless boundaries and zero normal velocities. The temperature difference between the top and the bottom boundary is fixed and on the sides we assume periodic boundaries (zero temperature fluxes). The domain is discretized into 710 six noded triangular elements with element concentrations along the sides of the model. Since the power law rheology is not yet implemented into our material point advection code ELLIPSIS (Moresi et al., 2001 [9]) we have used the finite element code Fastflo (see <http://www.cmis.csiro.au/Fastflo/> for more information). In Fastflo the user programs the mathematical model and algorithms by means of the high level language Fastalk. In the Fastflo macro developed for this application the momentum equilibrium equation based on the rheology (1) with the viscosity ratio as

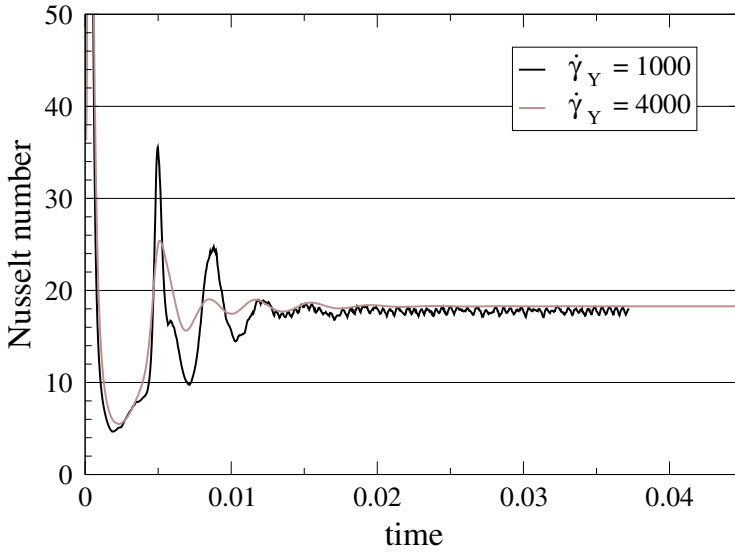


Fig. 3. Nusselt-number vs. time for a power law exponent of $n=5$ and dimensionless strain rates $\dot{\gamma}_Y = 1000$ (dark) and 4000 (light) respectively with steady state values of 17.8 and 18.5 respectively

defined by (7) is solved iteratively by successively substituting $\dot{\gamma}$ for a given temperature at each time step. An average of 4 iterations were required for four digit accuracy in the r.m.s. of the nodal point velocity vector.

Subsequently the heat equation is solved using a backward Euler differencing scheme and tensor upwinding. The latter amounts to the inclusion of an additional diffusion term with the diffusivity tensor $v_i v_j \Delta t / 2$ (Zienkiewicz and Taylor, [10]). Finally the director advection equation (3) is solved – again using an Euler backward scheme and tensor upwinding. Tensor upwinding is very important here, because of the hyperbolic nature of the director equation (see Fig. 5). The time-step is determined from the Courant condition-like criterion

$$\Delta t = \alpha \frac{\sqrt{\text{area}/2 \times \text{num. of elem.}}}{v_{max}}. \quad (14)$$

In the calculations we have assumed that $\alpha = 1/2$; The factor 2 in the numerator considers the fact that the elements are triangular. As in the other sections of this paper we assume an isotropic Rayleigh number of $Ra = 5.64 \times 10^5$, an initial temperature perturbation of

$$T = 1 - x_2 + \frac{1}{10} \cos(\pi x_1) \sin(\pi x_2), \quad (15)$$

and an initial director orientation of $\mathbf{n}^T = (0, 1)$ everywhere. Figure 3 shows the evolution of the Nusselt-number with time for a power law exponent of $n=5$ and dimensionless strain rates $\dot{\gamma}_Y = 1000$ and 4000 respectively. The steady state Nusselt numbers are 17.8

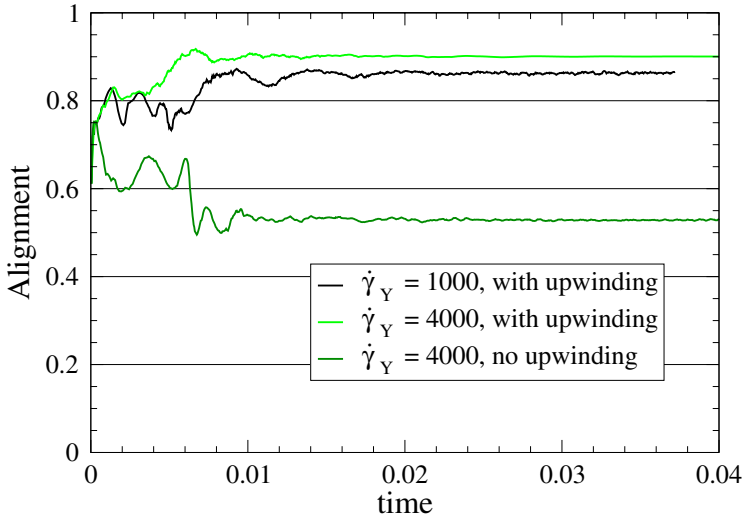


Fig. 4. Alignment for $\dot{\gamma}_Y = 1000$ (dark graph; with upwind) and $\dot{\gamma}_Y = 4000$ (medium; no upwind and light with upwind) respectively. The shear viscosity contrast and hence the anisotropy is largest in the up and down welling plumes. A milder degree of anisotropy is also observed in the cold and the hot boundary layers. The core of the convection cells is virtually isotropic

and 18.5 for $\dot{\gamma}_Y = 100$ and 4000 respectively. In the calculations we have used the definition

$$Nu = 1 + \frac{1}{Ra} \int_V \sigma_{ij} D_{ij} dV, \quad (16)$$

of the Nusselt number which is also valid during the transient phase of convection (see eg. Christensen, 1984 [4]). In Eq. (16) all quantities are non dimensional.

A global measure for the degree of alignment of the director in dependency of the time is represented in Fig. 4. For a quadratic domain of unit area the degree of alignment is measured in terms of the sin of the mean value of the angle enclosed by the velocity vector and the director:

$$\int_V |\sin(\alpha)| dV = \int_V \left(\frac{|v_1 n_2 - v_2 n_1|}{|\mathbf{v}| |\mathbf{n}|} \right) dV \quad (17)$$

If the velocity vector is everywhere orthogonal to the director (full alignment) then $\sin(\alpha) = 1$. In the simulations we achieve an average alignment of 0.85 and 0.91 for $\dot{\gamma}_Y = 1000$ and $\dot{\gamma}_Y = 4000$ respectively with tensor upwinding. Also shown is the alignment evolution for $\dot{\gamma}_Y = 1000$ without upwinding (purple graph in Fig. 4). In this case alignment does not take place because of the numerical ill-posedness of the unstabilised director equations.

Figure 5 (A) and (B) show the contours of the streamlines (determined in the usual way from the velocity potential ϕ where $v_1 = \phi_{,2}$ and $v_2 = -\phi_{,1}$) and the isotherms respectively; both plots are for $\dot{\gamma}_Y = 1000$. The streamlines lines are more angular than

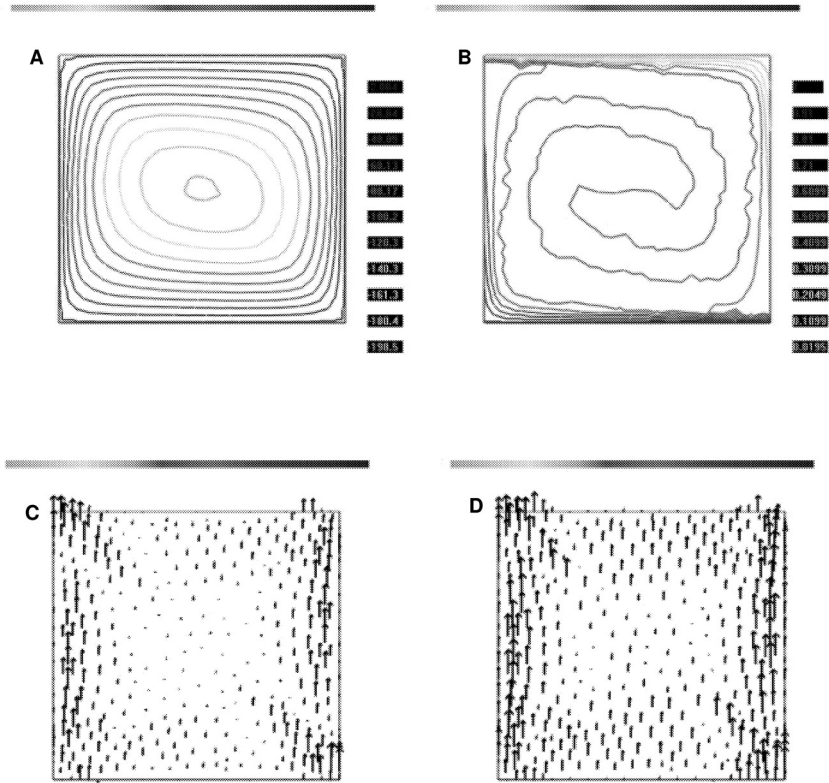


Fig. 5. Streamlines (A), isotherms (B) $n=5$ and $\dot{\gamma}_Y = 1000$ in (A) and (B). (C) and (D): pseudo vectors $(0, 1 - \eta_S/\eta)$; The arrows are normalized with respect to the maximum arrow length. Actual max arrow length: 0.57 (C), 0.93 (D); Parameters: $n=5$, $\dot{\gamma}_Y = 4000$ (C), $n=5$, $\dot{\gamma}_Y = 1000$ (D)

in isotropic convection. Also characteristic for anisotropic convection is the spiral like shape of the isotherms. An important measure for the spatial distribution of anisotropy is the distribution of ratio of η_S/η ; if $\eta_S/\eta = 1$ the material behaves locally isotropic; strong anisotropy is obtained for $\eta_S/\eta = 0$, i.e. in the limit $\dot{\gamma}/\dot{\gamma}_Y \rightarrow \infty$. In Fig. 5 the viscosity ratio is represented for visualization purposes by means of the distribution of the pseudo vector field $(0, 1 - \eta_S/\eta)$ anisotropy is strongest where the arrow is longest and *vice versa*. In the plots the vector are normalized such that the magnitudes range between 0 and 1. The actual magnitude ranges between 0.57 for $\dot{\gamma}_Y = 4000$ and 0.93 for $\dot{\gamma}_Y = 1000$. The anisotropy is strongest in both cases in the hot and cold plumes on the sides of the cell. The core of the convection cells are more or less isotropic however in the case of the lower transition strain rate we observe significant anisotropy (in terms of the viscosity ratio) in the vicinity of the hot and cold thermal boundary layers as well.

Acknowledgement. The authors gratefully acknowledge the support of the supercomputing facilities of the Australian Earth System Simulator (ACcESS), a Major National Research Facility.

References

1. Mühlhaus, H.-B., Dufour, F., Moresi, L., Hobbs, B., (2002) *A director theory for viscoelastic folding instabilities in multilayered rock*, Int. J. Solids and Structures. Vol. 39; 3675–3691.
2. Mühlhaus, H.-B., Moresi, L., Hobbs, B., Dufour, F., (2002) *Large Amplitude Folding in Finely Layered Viscoelastic Rock Structures*, Pure. Appl. Geophys., 159, 2311–2333
3. Christensen, U.C., (1987) *Some geodynamical effects of anisotropic viscosity*, Geophys.J.R.astr. Soc. 91;711-736.
4. U. Christensen (1984) Convection with pressure and temperature dependent non-Newtonian rheology. Geophys. J.R. Astr. Soc.,77, 343–384
5. Aki, K., (1968) *Seismological evidence for the existence of soft thin layers in the upper mantle under Japan*, J. Geophys. Res., 73, 585–596.
6. Karato, S.-I., (1998) *Seismic Anisotropy in the Deep Mantle, Boundary Layers and the Geometry of Mantle Convection*, Pure appl. geophys., 151, 565–587.
7. Montagner, J.-P., and Kennett, B.L.N., (1996) *How to Reconcile Body-wave and Normal-mode Reference Earth Model*, Geophys. J.. Int. 125, 229–248.
8. Takeuchi, H., Y. Hamano, and Y. Hasegawa, (1968) *Rayleigh- and Love-wave discrepancy and the existence of magma pockets in the upper mantle*, J. Geophys. Res., 73, 3349–3350.
9. Moresi, L., Mühlhaus, H.-B., Dufour, F., (2001) *Particle-in-Cell Solutions for Creeping Viscous Flows with Internal Interfaces*, Proceedings of the 5th International Workshop on Bifurcation and Localisation (IWBL'99), Perth, H.-B. Mühlhaus, A. Dyskin, E. Pasternak Australia, Balkema, Rotterdam.
10. O.C. Zienkiewicz and R.L. Taylor (2000), *Finite Element Method: Volume 3, Fluid Dynamics*; ISBN 0750650508, Butterworth-Heinemann).
11. C.J. Allegre and D.L. Turcotte (1986) Implications of two component marble cake mantle. Nature, 323, 123–127